



1 **Dynamics-based estimates of decline trend with fine temporal variations in China's**
2 **PM_{2.5} emissions**

3

4 **Zhen Peng^{1†}, Lili Lei^{1,2†}, Zhe-Min Tan^{1,2*}, Meigen Zhang^{3*}, Aijun Ding¹ and Xingxia Kou⁴**

5 ¹School of Atmospheric Sciences, Nanjing University, Nanjing 210093, China

6 ²Key Laboratory of Mesoscale Severe Weather, Ministry of Education, Nanjing University,
7 Nanjing 210093, China

8 ³State Key Laboratory of Atmospheric Boundary Layer Physics and Atmospheric Chemistry,
9 Institute of Atmospheric Physics, Chinese Academy of Sciences, Beijing 100029, China

10 ⁴Institute of Urban Meteorology, China Meteorological Administration, Beijing 100089, China

11

12 Corresponding author: Zhe-Min Tan (zmtan@nju.edu.cn) and Meigen Zhang
13 (mgzhang@mail.iap.ac.cn)

14

15 **Abstract**

16 Timely, continuous, and dynamics-based estimates of PM_{2.5} emissions with a high temporal
17 resolution can be objectively and optimally obtained by assimilating observed surface PM_{2.5}
18 concentrations using flow-dependent error statistics. Annual PM_{2.5} emissions in China have
19 consistently decreased of approximately 3% to 5% from 2017 to 2020. Significant PM_{2.5} emission
20 reductions occurred frequently in regions with large PM_{2.5} emissions. COVID-19 could cause a
21 significant reduction of PM_{2.5} emissions in the north China plain and northeast of China in 2020.
22 The magnitudes of PM_{2.5} emissions were greater in the winter than in the summer. PM_{2.5} emissions
23 show an obvious diurnal variation that varies significantly with the season and urban population.
24 Improved representations of PM_{2.5} emissions across time scales can benefit emission inventory,
25 regulation policy and emission trading schemes, particularly for especially for high temporal



26 resolution air quality forecasting and policy response to severe haze pollutions or rare human
27 events with significant socioeconomic impacts.

28

29 **1. Introduction**

30 Anthropogenic emissions have imposed essential influences on the earth system, from
31 hourly air quality and human health to long-time climate and environment. To reduce
32 anthropogenic emissions, the Chinese government has enforced the Clean Air Action (2013) since
33 2013. Studies to date that evaluated the emission controls and understood the climate responses
34 from emission reductions often have used either a fixed meteorology with emission changes or
35 *vice versa* (Li et al., 2019a; Li et al., 2021, Zhai et al., 2021). Estimated emissions from empirical
36 extrapolation were commonly applied to analyze the meteorological-chemical mechanisms and
37 associated social-economic impacts from occasional events like the 2015 China Victory Day
38 Parade and Coronavirus Disease 2019 (COVID-19) pandemic (Wang et al., 2017; Liu et al., 2020;
39 Huang et al., 2020; Zhu et al., 2021). But to better understand both long-term and short-term
40 influences from emission changes, the continuous, up-to-date, and high temporal-/spatial-
41 resolution emission estimates with coherent interactions of meteorology and emission changes are
42 needed.

43 The complex contributions from energy production, industrial processes, transportation,
44 and residential consumptions have imposed great challenges to accurately estimate the emissions.
45 The emission inventories created by the traditional bottom-up techniques were typically outdated
46 from the present day due to the lack of accurate and timely statistics, and often with coarse
47 temporal resolutions from monthly to annual (Zhang et al., 2009; Li et al., 2014; Janssens-
48 Maenhout et al., 2015; Zheng et al., 2018). Alternatively, update-to-date emission estimates with
49 high temporal-spatial resolutions could be provided by top-down techniques (Miyazaki et al.,
50 2017), but most emissions estimated by top-down techniques were intermittent and analyzed at
51 monthly scale or longer longer (Zhang et al., 2016; Jiang et al., 2017; Qu et al., 2017; Cao et al.,
52 2018; Müller et al., 2018; Chen et al., 2019; Li et al., 2019b; Miyazaki et al., 2020). Moreover,
53 emissions updated by the top-down techniques based on satellite observations could be insufficient
54 to capture realistic near-surface characteristics (Li et al., 2019b; Liu et al., 2011; Choi et al., 2020).



55 Given the development of observation networks and advanced data assimilation strategies,
56 timely and dynamics-based emission estimates with high temporal resolution can be achieved by
57 harmonically constraining the atmospheric-chemical model with dense observations of trace gas
58 compounds through an optimal assimilation methodology. The ensemble Kalman smoother (EnKS)
59 (Whitaker et al., 2002; Peters et al., 2007; Peng et al., 2015), as a four-dimensional (4D)
60 assimilation algorithm, makes use of chemical observations from past to future to provide an
61 optimal estimate of source emissions, and it can capture the “error of the day” and construct fine
62 emission characteristics with high temporal-spatial resolutions by using short-term ensemble
63 forecasts (Kalnay, 2002). Since 2013, the fine particulate matter pollution (PM_{2.5}, particles smaller
64 than 2.5 μm in diameter) as the most urgent threat to public health has been persistently decreased,
65 and ground-based observations of PM_{2.5} have been progressively increased (Huang et al., 2018).
66 Thus by harmonically assimilating dense surface PM_{2.5} observations into an atmospheric-chemical
67 model through an EnKS, hourly estimates of PM_{2.5} emission that were continuously cycled for
68 years 2016-2020 are presented in this study.

69 The timely estimated emissions can provide guidance for emission inventories that usually
70 have time lags and emission trading schemes that often require up-to-date source emissions. Based
71 on the dynamics-based estimated emissions with harmonic combination of the model and
72 observations, better evaluation of the emission controls and more comprehensive understanding of
73 the consequent climate responses can be obtained. The high temporal-resolution estimated
74 emissions can reveal features of emissions that are absent from the traditional ones with coarse
75 temporal resolutions. Moreover, the timely and dynamics-based emission estimates with high
76 temporal resolution are essential for regional air quality modeling, especially for the occurrence of
77 severe haze pollutions associated with timely evaluation for the impact on public health (Attri et
78 al., 2001; Wang et al., 2014; Ji et al., 2018; Wang et al., 2020; Liu et al., 2021) and events that
79 lead to large changes of emissions and significant socioeconomic impacts such as the COVID-19
80 pandemic (Huang et al., 2020; Le et al., 2020).

81 **2. Data assimilation and experimental design**

82 The estimate of PM_{2.5} emission can be successfully constrained by the PM_{2.5} concentration
83 observations through an ensemble Kalman filter (EnKF; Peng et al., 2017, 2018, 2020). For a
84 retrospective ‘reanalysis’ mode here, all available PM_{2.5} concentration observations, including



85 those data collected after the analysis time, can be used. Thus a EnKS, a direct generalization of
 86 the EnKF, is applied to incorporate PM_{2.5} concentration observations both before and after the
 87 analysis time, aiming to provide an optimal estimate of the PM_{2.5} emission. Detailed procedures
 88 of the EnKS are described in section 2.1.

89 **2.1 An ensemble Kalman smoother to update the source emission**

90 The ensemble priors of source emissions \mathbf{e}^f is created by multiplying a scaling factor λ^f
 91 to the prescribed emission \mathbf{e}^p (Peng et al., 2017, 2018, 2020), where the superscript f denotes
 92 priors. Given a constant \mathbf{e}^p , the update of \mathbf{e}^f is equivalent to the update of λ^f . Due to a time lag,
 93 the prior scaling factor at time $t-1$ (λ_{t-1}^f) is updated by chemical observations at time t (\mathbf{y}_t^c). At time
 94 $t-1$, the prior scaling factor for the i^{th} member is written as

$$95 \quad \lambda_{i,t-1}^f = \frac{1}{M} \left[\left(\beta \frac{\mathbf{c}_{i,t-1}^f}{\bar{\mathbf{c}}_{t-1}^f} + 1 - \beta \right) + \sum_{j=t-M}^{t-2} \lambda_{i,j|j+1:t-1}^a \right] \quad (1)$$

96 The first term is the concentration ratio given by the prior of the chemical fields ($\mathbf{c}_{i,t-1}^f$) normalized
 97 by the ensemble mean ($\bar{\mathbf{c}}_{t-1}^f$), where β is an inflation factor used to compensate the insufficient
 98 ensemble spread (Peng et al., 2017). Through using the concentration ratio, each ensemble member
 99 of the source emissions naturally has the spatial correlations given by the chemical fields. The
 100 second term is the mean of the posterior scaling factors at previous assimilation cycles, where the
 101 superscript a denotes posteriors, M is the length of smoothing, and the subscript $j+1:t-1$ indicates
 102 that the scaling factor at time j is updated by future observations from $j+1$ to $t-1$. The assimilation
 103 of future observations will be described below.

104 The ensemble square-root filter (EnSRF) (Peng et al., 2017) is used to update $\lambda_{i,t-1}^f$ by
 105 assimilating \mathbf{y}_t^c . For the scaling factor at time $t-1$, posterior ensemble mean is given by

$$106 \quad \bar{\lambda}_{t-1}^a = \bar{\lambda}_{t-1}^f + \rho \circ \mathbf{P}_{t-1,t}^{ec} \mathbf{H}_t^{cT} \left(\mathbf{H}_t^c \mathbf{P}_t^c \mathbf{H}_t^{cT} + \mathbf{R}_t^c \right)^{-1} \left(\mathbf{y}_t^c - \mathbf{H}_t^c \bar{\mathbf{c}}_t^f \right), \quad (2)$$

107 and posterior ensemble perturbations are given by



$$108 \quad \lambda_{i,t-1}^a = \lambda_{i,t-1}^f - \rho \circ \mathbf{P}_{t-1,t}^{ec} \mathbf{H}_t^{cT} \left[\left(\sqrt{\mathbf{H}_t^c \mathbf{P}_t^c \mathbf{H}_t^{cT} + \mathbf{R}_t^c} \right)^{-1} \right]^T \left[\sqrt{\left(\mathbf{H}_t^c \mathbf{P}_t^c \mathbf{H}_t^{cT} + \mathbf{R}_t^c \right) + \sqrt{\mathbf{R}_t^c}} \right]^{-1} \mathbf{H}_t^c \lambda_{i,t-1}^f, \quad (3)$$

109 (3)

110 where $\mathbf{P}_{t-1,t}^{ec}$ denotes the background error covariance matrix of $\lambda_{i,t-1}^f$ and \mathbf{c}_t^f , \mathbf{P}_t^c indicates the
 111 background error covariance matrix of \mathbf{c}_t^f , H_t^c , \mathbf{H}_t^c and \mathbf{R}_t^c are the observation forward operator,
 112 Jacobian matrix and observation error covariance matrix of the chemical fields at time t , ρ is the
 113 localization matrix and \circ denotes the Schur (elementwise) product.

114 By applying the ensemble Kalman smoother (EnKS) (Whitaker et al., 2002; Peters et al.,
 115 2007), the chemical observation y_t^c is also assimilated to update the posterior scaling factor at
 116 previous assimilation cycles $j (j = t - K, \dots, t - 2)$. After assimilating the future chemical
 117 observation at time t , posterior ensemble mean of the scaling factor at j is given by

$$118 \quad \bar{\lambda}_{j|j+t}^a = \bar{\lambda}_{j|j+t-1}^a + \rho \circ \mathbf{P}_{j|j+t-1,t}^{ec} \mathbf{H}_t^{cT} \left(\mathbf{H}_t^c \mathbf{P}_t^c \mathbf{H}_t^{cT} + \mathbf{R}_t^c \right)^{-1} \left(y_t^c - H_t^c \bar{\mathbf{c}}_t^f \right), \quad (4)$$

119 and posterior ensemble perturbations are given by

$$120 \quad \lambda_{i,j|j+t}^a = \lambda_{i,j|j+t-1}^a - \rho \circ \mathbf{P}_{j|j+t-1,t}^{ec} \mathbf{H}_t^{cT} \left[\left(\sqrt{\mathbf{H}_t^c \mathbf{P}_t^c \mathbf{H}_t^{cT} + \mathbf{R}_t^c} \right)^{-1} \right]^T \left[\sqrt{\left(\mathbf{H}_t^c \mathbf{P}_t^c \mathbf{H}_t^{cT} + \mathbf{R}_t^c \right) + \sqrt{\mathbf{R}_t^c}} \right]^{-1} \mathbf{H}_t^c \lambda_{i,t-1}^f, \quad (5)$$

121 where $\mathbf{P}_{j|j+t-1,t}^{ec}$ denotes the background error covariance matrix of $\lambda_{j|j+t-1}^a$ and \mathbf{c}_t^f . After (2)-(5),
 122 the updated $\lambda_{j|j+t}^a$, $j (j = t - M + 1, \dots, t - 1)$ will be used to construct the prior scaling factor at next
 123 time $t+1$ (1).

124 As a Monte Carlo approach, the EnKS uses the forecast-analysis error covariances based
 125 on ensemble forecasts / analyses to compute the Kalman gain matrix with time lags, to incorporate
 126 observations from the past to the future. The first iteration of EnKS is equivalent to EnKF that
 127 assimilates observations up to the analysis time. The following iterations of EnKS assimilate
 128 observations in the future to update the state at the analysis time. The hourly forecasts of PM_{2.5}
 129 concentration from the cycling assimilation experiment matched the independent observed



130 quantities (Figure 1). Therefore, the ability of EnKS to retrieve the source emissions has been
131 demonstrated.

132 **2.2 WRF-Chem model, observations and emissions**

133 To simulate the transport of aerosol and chemical species, the WRF-Chem model version
134 3.6.1 (Grell et al., 2005) that has the meteorological and chemical components fully coupled is
135 used. The model parameterization schemes follow Peng et al. (2017). Figure 2 shows the model
136 domain that covers most east Asia regions. Horizontal grid spacing is 45 km with 57 vertical levels
137 and model top at 10 hPa.

138 Experiments are conducted for each year from 2016 to 2020 separately. The 6-h
139 meteorological observations, including all in-situ observations and cloud motion vectors from the
140 National Centers for Environmental Prediction (NCEP) Global Data Assimilation System (GDAS;
141 http://www.emc.ncep.noaa.gov/mmb/data_processing/prepbufr.doc/table_2.htm), are assimilated
142 every 6 h. The hourly observed chemical quantities, which contain PM₁₀, PM_{2.5}, SO₂, NO₂, O₃,
143 and CO from the Ministry of Ecology and Environment of China (<https://aqicn.org/map/china/cn/>),
144 are assimilated every hour. Figure 2 shows the assimilated chemical observation network, which
145 has 560 randomly chosen stations from 1576 stations in total. The thinning of observations is
146 applied to avoid correlated errors of observations (Peng et al., 2017). The observation priors are
147 computed by the “observer” portion of the Grid-point Statistical Interpolation system (GSI) (Kleist
148 et al., 2009).

149 The hourly and constantly prescribed anthropogenic emissions are obtained from the
150 EDGAR-HTAP (Emission Database for Global Atmospheric Research for Hemispheric Transport
151 of Air Pollution v2.2) v2.2 inventory (Janssens-Maenhout et al., 2015), in which the Chinese
152 emissions are derived from MEIC in 2010 (Lei et al., 2011; Li et al., 2014). Natural emissions,
153 including the biogenic (Guenther et al., 1995), dust (Ginoux et al., 2001), dimethyl sulfide and sea
154 salt emissions (Chin et al., 2000), are computed online.

155 **2.3 Assimilation and ensemble configurations**

156 The PM_{2.5} emission directly gives the primary PM_{2.5}, and then the primary PM_{2.5} along
157 with other precursor emissions could contribute to the secondary PM_{2.5}. The observations of PM_{2.5}
158 concentrations that contain both primary and secondary PM_{2.5}, are used to constrain the PM_{2.5}



159 emission through data assimilation. Thus the correlations between the concentration observations
160 and source emissions might be contaminated by the secondary $PM_{2.5}$. In the present study, the
161 impact of the secondary $PM_{2.5}$ is ignored. One possible way to untangle the impact of secondary
162 $PM_{2.5}$ on the estimates of $PM_{2.5}$ emission is to jointly estimate the source emission, primary and
163 secondary $PM_{2.5}$ given the concentration observations.

164 The National Oceanic and Atmospheric Administration (NOAA) operational EnKF system
165 (https://dtcenter.ucar.edu/com-GSI/users/docs/users_guide/GSIUserGuide_v3.7.pdf), which is an
166 EnSRF and modified with the EnKS feature, is used to assimilate the observations. Ensemble size
167 is set to 50. To combat the sampling error resulted from a limited ensemble size, covariance
168 localization and inflation are applied. The Gaspari and Cohn (GC) (1999) function with a length
169 scale of 675 km is used to localize the impact of observations and mitigate the spurious error
170 correlations between observations and state variables. The constant multiplicative posterior
171 inflation (Whitaker and Hamill 2012) with coefficients 1.12 for all meteorological and chemical
172 variables is applied to enlarge the ensemble spread. The inflation β for advancing the scale factor
173 is 1.2. The smoothing length M for source emissions is 4, and the EnKS lagged length K is 6.

174 At 0000 UTC 26 December of previous year, ensemble initial conditions (ICs) of the
175 meteorological fields are generated by adding random perturbations that sample the static
176 background error covariances (Barker et al., 2012) on the NCEP FNL (Final) analyses (Torn et al.,
177 2006). Ensemble ICs of the chemical fields are 0, and source emissions of each ensemble member
178 are adopted from the EDGAR-HTAP v2.2 inventory with random perturbations of mean 0 and
179 variances of 10% of the emission values. Hourly ensemble lateral boundary conditions (LBCs) are
180 generated using the same fixed-covariance perturbation technique as the ensemble ICs. After 6-d
181 spin up, ensemble data assimilation experiments start cycling for each year.

182 **3. $PM_{2.5}$ emission for years 2016-2020**

183 Starting from the constant source emission PR2010 (Janssens-Maenhout et al., 2015), the
184 annual dynamics-based estimates of $PM_{2.5}$ emission (DEPE) averaged over mainland China for
185 years 2016-2020 are 8.17, 7.91, 7.53, 7.13 and 6.89 Tg, respectively. For years 2016 and 2017, the
186 annual DEPE are very closed to 8.1 and 7.6 Tg from the Multi-resolution Emission Inventory
187 (MEIC) (Zheng et al., 2018). From year 2017 to 2020, the estimated annual $PM_{2.5}$ emissions are
188 reduced 3.2%, 7.8%, 12.7% and 15.7% respectively compared to that of year 2016. There has been



189 3%-5% persistent reduction of annual $PM_{2.5}$ emission from year 2017 to 2020, which demonstrates
190 the effectiveness of China's Clean Air Action (2013) implemented since 2013 and China Blue Sky
191 Defense War Plan (2018) enforced since 2018 with strengthened industrial emission standards,
192 phased out outdated industrial capacities, promoted clean fuels in residential sector and so on
193 (Zhang et al., 2019).

194 The monthly DEPE show reduction of $PM_{2.5}$ emission nearly in each month from years
195 2016 to 2020 (Figure 3a), which further demonstrates the effectiveness of China's national plan,
196 rather than the role of weather effects alone. Compared to year 2016, both the reduction amount
197 and reduction ratio of $PM_{2.5}$ emission are more prominent for February, March, June-September,
198 and November than the other months (Figure 3b). Given larger magnitudes of $PM_{2.5}$ emission in
199 winter than in summer, emission controls with a focus from October to May should be considered
200 in the design of future clean air actions in China, since total $PM_{2.5}$ emission during this period
201 accounts for approximate 75% annual amount. Spatial distributions of the changes of $PM_{2.5}$
202 emission from year 2017 to 2020 compared to year 2016 show significant decreases occurred at
203 Beijing-Tianjin-Hebei region (BTH), Yangtze River Delta region (YRD), Pearl River Delta region
204 (PRD) and Sichuan-Chongqing Region (SCR), especially for years 2019-2020 (Figure 4). From
205 year 2016 to 2020, BTH, YRD and SRC have larger reductions of $PM_{2.5}$ emission than PRD, but
206 SCR has larger reduction ratio compared to year 2016 than BTH and YRD (Figure 5). Therefore,
207 BTH and YRD have more potentials for $PM_{2.5}$ emission controls than PRD and SCR, which can
208 give a guidance for future clean air actions. More specifically, most provinces have $PM_{2.5}$ emission
209 reduction from year 2016 to 2020, and the reduction ratios generally increase from year 2017 to
210 2020 (Table 1), which confirms continuous and effective emission controls from Clean Air Action
211 to Blue Sky Defense War Plan in China.

212 Despite the trend in $PM_{2.5}$ emissions from year 2016 to 2020, the DEPE of year 2016 has
213 similar monthly distributions to MEIC2016 in general (Figure 3a). MEIC2016 has a "Pan-shape"
214 monthly distribution with nearly constant $PM_{2.5}$ emissions from April to October. This seasonal
215 dependence of emissions is mainly contributed by the variations of residential energy use, which
216 are empirically dependent on coarse monthly mean temperature intervals and thus cannot reflect
217 the realistic monthly variations (Streets et al., 2003; Li et al., 2017). However, the DEPE yet shows
218 a "V-shape" monthly distribution, with the minimum occurring in August. The estimated $PM_{2.5}$
219 emission is 11.8% higher than MEIC2016 in April but 12.1% lower than MEIC2016 in August,



220 and these different monthly distributions can influence the consequent climate responses including
221 the radiative forcing and energy budget (Yang et al., 2020) and also impact the health issues (Liu
222 et al., 2018). Moreover, monthly fractions of the DEPE are consistent cross years (Figure 3c). The
223 absence of interannual variations of monthly $PM_{2.5}$ emission fraction provides basis for previous
224 studies that follow the same monthly changes of source emissions from different years (Zhang et
225 al., 2009; Zheng et al., 2020, 2021). Monthly allocations of $PM_{2.5}$ emission can be directly and
226 objectively obtained given an estimated total annual amount based on the estimated monthly
227 fractions of DEPE, which is valuable for emission inventory, air quality simulation, and potentially
228 applications for future scenarios due to more accurate month fractions of DEPE. Since the hourly
229 priors of $PM_{2.5}$ concentrations from the cycling assimilation for optimally estimating $PM_{2.5}$
230 emission fit to the observed $PM_{2.5}$ quantities (Figure 1), the monthly DEPE provides more realistic
231 monthly fluctuations than the empirical estimate.

232 **4. Diurnal variations of $PM_{2.5}$ emission**

233 The DEPE with high temporal-resolution given the constant prior PR2010 can reveal
234 features that are unable to represent in the commonly used emission estimates. Although the prior
235 PR2010 has no diurnal variations, hourly posteriors of $PM_{2.5}$ emission provide the first objectively
236 estimated diurnal variations for different seasons for years 2016-2020. To statistically present the
237 diurnal variations, the fractions of hourly $PM_{2.5}$ emissions divided by the daily amount are
238 averaged over different years and regions (Figures 6 and 7, and Table 2). The diurnal variations of
239 $PM_{2.5}$ emission are critical for understanding the mechanisms of $PM_{2.5}$ formation and evolution
240 and are also essential for $PM_{2.5}$ simulation and forecast.

241 Five-year mean diurnal variations of the estimated $PM_{2.5}$ emission fraction for mainland
242 China show that despite the monthly variations of $PM_{2.5}$ emission, the diurnal-variation fractions
243 for November, December, January and February are similar, while those for June, July and August
244 are similar (Figure 6a). There are stronger diurnal variations of $PM_{2.5}$ emission in summer than in
245 winter, which are represented by larger $PM_{2.5}$ emission fractions during morning and less $PM_{2.5}$
246 emission fractions during evening. The diurnal variations of $PM_{2.5}$ emission from March to May
247 gradually transform from the patterns of winter to those of summer, and *vice versa* for the diurnal
248 variations of $PM_{2.5}$ emission from September to November. The monthly changes of diurnal
249 variations of $PM_{2.5}$ emission are consistent with the seasonal dependence, since monthly variations



250 of $PM_{2.5}$ emission are mainly related to the variations of residential consumptions (Li et al., 2017)
251 in which the space-heating has nearly no diurnal variations and then larger $PM_{2.5}$ emissions during
252 winter lead to reduced diurnal variations than summer. Similar to the monthly fractions of
253 estimated $PM_{2.5}$ emission for mainland China, diurnal variations of $PM_{2.5}$ emission fraction are
254 consistent cross years for a given month (Figure 7). Table 2 gives five-year mean diurnal variations
255 of the estimated $PM_{2.5}$ emission fraction for each month. Based on these high-resolution diurnal-
256 variation fractions, hourly estimates of $PM_{2.5}$ emission can be objectively obtained for a given
257 monthly estimated $PM_{2.5}$ emission.

258 Despite the high temporal resolution, the DEPE also has the ability to analyze diurnal
259 variations for specific cities. The monthly changes of diurnal variations of $PM_{2.5}$ emission
260 estimated for megacities with urban populations larger than 5 million and non-megacities with
261 urban populations smaller than 5 million (Notice of the State Council on Adjusting the Standards
262 for Categorizing City Sizes, 2014) are consistent with those estimated from mainland China
263 (Figure 6). Compared to the diurnal variations of $PM_{2.5}$ emission estimated for mainland China,
264 the megacities have stronger diurnal variations, while the non-megacities have weaker diurnal
265 variations. These detailed descriptions of $PM_{2.5}$ emission that are usually absent in common
266 emission estimates can be essential for $PM_{2.5}$ simulation, especially for providing timely and
267 realistic guidance for severe haze events.

268 There has been lack of local measurements for diurnal variations and widely adopted
269 diurnal variation profiles of $PM_{2.5}$ emission in China. Compared to the diurnal variations of $PM_{2.5}$
270 emission fractions estimated based on diurnal variation profiles from US and EU (Wang et al.,
271 2010), the noon and evening peaks estimated from DEPE have smaller $PM_{2.5}$ emission fractions,
272 with mean underestimations of $PM_{2.5}$ emission fraction of 0.31% and 1.05% for noon peak and
273 evening peak respectively (Figures 6a and 8). The morning peak of Wang et al. (2010) is similar
274 to that of DEPE for spring and fall, but the former overestimates $PM_{2.5}$ emission fraction of 0.81%
275 for winter while underestimates $PM_{2.5}$ emission fraction of 0.79% for summer. Due to the
276 overestimated peaks, diurnal variations of Wang et al.(2010) have sharper appearance rate for
277 morning peak and disappearance rate for evening peak. Compared to the diurnal variations based
278 on diurnal variation profiles from ES and EU (Wang et al., 2010), the diurnal variations of the
279 DEPE are constrained by the atmospheric-chemical model and observed $PM_{2.5}$ concentrations,



280 which can objectively determine the diurnal variations of PM_{2.5} emission for specific regions and
281 seasons.

282 **5. Impact of COVID-19 on PM_{2.5} emissions**

283 The abrupt outbreak of the COVID-19 pandemic has produced dramatically socioeconomic
284 impacts in China. To prevent the virus spread, a lockdown was first implemented on 23 January
285 2020 in Wuhan, Hubei province, and subsequently the national lockdown has been enforced in
286 China (Liu et al., 2020; Huang et al., 2020; Zhu et al., 2021). Consequently, the total PM_{2.5}
287 emission of February 2020 for China shows an obvious decrease compared to those of previous
288 years (Figure 3). The high temporal-resolution DEPE reveals the detailed changes of PM_{2.5}
289 emission with time (Figure 9). The PM_{2.5} emission started to decrease right around the COVID
290 outbreak, and had been smaller than those of year 2019 till early March. During February 2020,
291 the DEPE shows significant reductions at the north China plain and northeast of China where
292 prominent PM_{2.5} emission occurred, while spotted PM_{2.5} emission differences with small
293 magnitudes showed at the other regions (Figures 10a-b). Along with recovery from the COVID-
294 19, the estimated PM_{2.5} emission rebounded in March (Figures 3a, 9, 10c-d), which is contributed
295 to the national work resumption. Thus, the DEPE is able to timely reflect the dynamic response of
296 PM_{2.5} emission to the COVID-19.

297 To avoid fluctuations due to diurnal variations and monthly changes of PM_{2.5} emission, 7-
298 day averaged PM_{2.5} emission differences between year 2020 and 2019 are used to analyze the
299 dynamic impact of COVID-19 on PM_{2.5} emission (Figure 11). Before the lockdown, there were
300 slight PM_{2.5} emission differences over several provinces (Figures 11a-b). During the first week of
301 lockdown, PM_{2.5} emission reduction larger than 5×10^{-2} ($\mu\text{g} \cdot \text{m}^{-2} \cdot \text{s}^{-1}$) that is about 60%-70%
302 emission reduction, occurred at Hubei, Hunan, Guangdong, Anhui and Zhejiang provinces (Figure
303 11c). The PM_{2.5} emission reduction extended to BTH and Shandong province during the second
304 week of lockdown (Figure 11d), and continuously spread to the three northeast provinces of China
305 during the third week of lockdown (Figure 11e). During the third week of lockdown, the increased
306 PM_{2.5} emissions for BTH and SCR are possibly caused by the massive emissions from high-profile
307 firework burning on the Chinese New Year Eve of year 2019 (Ji et al., 2018). The PM_{2.5} emission
308 reduction had been maintained over the central and northern China till early March when the



309 lockdown was lift (Figures 11f-i). Thus, the timely DEPE can provide up-to-date guidance for
310 quantifying

311 **6. Discussion**

312 High temporal-resolution and dynamics-based estimations of $PM_{2.5}$ emission can be
313 objectively and optimally obtained by assimilating past and future observed surface $PM_{2.5}$
314 concentrations through flow-dependent error statistics. This advanced assimilation strategy can be
315 applied for emission estimates of other chemical species when corresponding observations are
316 available, and extend to observation types besides the surface concentrations, like the aerosol
317 optical depth (Liu et al., 2011; Choi et al., 2020). Moreover, current estimates of $PM_{2.5}$ emission
318 are lack of explicitly representations of primary and secondary $PM_{2.5}$, which could be resolved by
319 joint estimation of the source emission, primary and secondary $PM_{2.5}$ given the concentration
320 observations. Another deficiency of this top-down technique is that it cannot directly determine
321 dynamics-based $PM_{2.5}$ emissions for different sectors as the bottom-up techniques. But this top-
322 down technique can be integrated into the bottom-up technique to retain advantages of both
323 methods. The annual emission estimate from the bottom-up technique can be further downscaled
324 to hourly estimates by first distributing the annual amount to each month through the monthly
325 allocations estimated from the top-down technique, and then assuming evenly daily distribution,
326 finally applying the fractions of diurnal variation estimated from the top-down technique. The
327 information collected by the bottom-up technique is retained, while the common drawback of
328 coarse temporal resolution for the bottom-up technique is remedied. The integrated bottom-up and
329 top-down technique can improve spatiotemporal representations of source emissions cross time
330 scales and sectors, which is beneficial for emission inventory, air quality forecast, regulation policy
331 and emission trading scheme.

332

333 **Acknowledgments**

334 This work is jointly sponsored by the National Key R&D Program of China through Grant
335 2017YFC1501603 and the National Natural Science Foundation of China through Grants
336 41922036 and 42275153. We are grateful to the High Performance Computing Center of Nanjing
337 University for doing the cycling ensemble assimilation experiments.



338 **Data availability**

339 The meteorological data used for meteorological initial conditions and boundary conditions
340 is available from the University Corporation for Atmospheric Research (UCAR) Research Data
341 Archive (<https://rda.ucar.edu/datasets/ds083.3/>). The assimilated meteorological observations are
342 available from the UCAR Research Data Archive (<https://rda.ucar.edu/datasets/ds337.0/>), and the
343 assimilated chemical observations are available from <https://aqicn.org/map/china/cn/>. The
344 prescribed constant anthropogenic emissions are available from the Emission Database for Global
345 Atmospheric Research for Hemispheric Transport of Air Pollution (EDGAR-HTAP) inventory
346 (https://data.jrc.ec.europa.eu/dataset/jrc-edgar-htap_v2-2) and the Multi-resolution Emission
347 Inventory (MEIC; http://meicmodel.org/?page_id=560).

348 The WRF-Chem model version 3.6.1 is available from
349 https://www2.mmm.ucar.edu/wrf/users/download/get_sources.html#WRF-Chem. The NOAA
350 operational EnKF system is available from [https://dtcenter.org/community-code/gridpoint-](https://dtcenter.org/community-code/gridpoint-statistical-interpolation-gsi)
351 [statistical-interpolation-gsi](https://dtcenter.org/community-code/gridpoint-statistical-interpolation-gsi).

352

353 **Competing interests**

354 The contact author has declared that none of the authors has any competing interests.

355

356 **References**

- 357 Attri, A. K., Kumar, U., and Jain, V. K.: Microclimate: formation of ozone by fireworks, *Nature*, 411, 1015,
358 2001.
- 359 Barker, D., Huang, X.-Y., Liu, Z., Auligné, T., Zhang, X., Rugg, S., Ajjaji, R., Bourgeois, A., Bray, J., Chen,
360 Y., Demirtas, M., Guo, Y.-R., Henderson, T., Huang, W., Lin, H.-C., Michalakes, J., Rizvi, S., and
361 Zhang, X.: The Weather Research and Forecasting Model's Community Variational/Ensemble Data
362 Assimilation System: WRFDA, *B. Am. Meteorol. Soc.*, 93, 831–843, [https://doi.org/10.1175/BAMS-](https://doi.org/10.1175/BAMS-D-11-00167.1)
363 [D-11-00167.1](https://doi.org/10.1175/BAMS-D-11-00167.1), 2012.
- 364 Cao, H., Fu, T.-M., Zhang, L., Henze, D. K., Miller, C. C., Lerot, C., Abad, G. G., De Smedt, I., Zhang, Q., van
365 Roozendael, M., Hendrick, F., Chance, K., Li, J., Zheng, J., and Zhao, Y.: Adjoint inversion of Chinese
366 non-methane volatile organic compound emissions using space-based observations of formaldehyde
367 and glyoxal, *Atmos. Chem. Phys.*, 18, 15017–15046, <https://doi.org/10.5194/acp-18-15017-2018>, 2018.



- 368 Chen, C., Dubovik, O., Henze, D. K., Chin, M., Lapyonok, T., Schuster, G. L., Ducos, F., Fuertes, D., Litvinov,
369 P., Li, L., Lopatin, A., Hu, Q., and Torres, B.: Constraining global aerosol emissions using
370 POLDER/PARASOL satellite remote sensing observations, *Atmos. Chem. Phys.*, 19, 14585–14606,
371 <https://doi.org/10.5194/acp-19-14585-2019>, 2019.
- 372 Chin, M., Rood, R. B., Lin, S. J., Muller, J. F., and Thompson, A. M.: Atmospheric sulfur cycle simulated in the
373 global model GO-CART: Model description and global properties, *J. Geophys. Res.-Atmos.*, 105,
374 24671–24687, 2000.
- 375 Choi, Y., Chen, S. H., Huang, C. C., Earl, K., Chen, C. Y., Schwartz, C. S., and Matsui, T.: Evaluating the impact
376 of assimilating aerosol optical depth observations on dust forecasts over North Africa and the East
377 Atlantic using different data assimilation methods, *Journal of Advances in Modeling Earth Systems*,
378 12(4), e2019MS001890. <https://doi.org/10.1029/2019ms001890>, 2020.
- 379 Gaspari, G. and Cohn S. E.: Construction of correlation functions in two and three dimensions, *Q. J. Roy. Meteor.*
380 *Soc.*, 125, 723–757, 1999.
- 381 Ginoux, P., Chin, M., Tegen, I., Prospero, J. M., Holben, B., Dubovik, O., and Lin, S.-J.: Sources and
382 distributions of dust aerosols simulated with the GOCART model, *J. Geophys. Res.*, 106, 20255–20273,
383 doi:10.1029/2000JD000053, 2001.
- 384 Grell, G., Peckham, S. E., Schmitz, R., McKeen, S. A., Frost, G., Skamarock, W. C., and Eder, B.: Fully coupled
385 “online” chemistry within the WRF model, *Atmos. Environ.*, 39, 6957–6975,
386 <https://doi.org/10.1016/j.atmosenv.2005.04.027>, 2005.
- 387 Guenther, A., Hewitt, C. N., Erickson, D., Fall, R., Geron, C., Graedel, T., Harley, P., Klinger, L., Lerdau, M.,
388 McKay, W., Pierce, T., Scholes, B., Steinbrecher, R., Tallamraju, R., Taylor, J., and Zimmerman, P.: A
389 global model of natural volatile organic compound emissions, *J. Geophys. Res.*, 100, 8873–8892,
390 doi:10.1029/94JD02950, 1995.
- 391 Huang, X., Ding, A., Gao, J., Zheng, B., Zhou, D., Qi, X., Tang, R., Wang, J., Ren, C., Nie, W., Chi, X., Xu, Z.,
392 Chen, L., Li, Y., Che, F., Pang, N., Wang, H., Tong, D., Qin, W., Cheng, W., Liu, W., Fu, Q., Liu, B.,
393 Chai, F., Davis, S. J., Zhang, Q., and He, K.: Enhanced secondary pollution offset reduction of primary
394 emissions during COVID-19 lockdown in China, *Natl. Sci. Rev.*, nwa137,
395 <https://doi.org/10.1093/nsr/nwaa137>, 2020.
- 396 Huang, J., Pan, X. C., Guo, X. B., and Li, G. X.: Health impact of China's Air Pollution Prevention and Control
397 Action Plan: an analysis of national air quality monitoring and mortality data, *Lancet Planet. Health*, 2,
398 E313–E323, [https://doi.org/10.1016/S2542-5196\(18\)30141-4](https://doi.org/10.1016/S2542-5196(18)30141-4), 2018.
- 399 Janssens-Maenhout, G., Crippa, M., Guizzardi, D., Dentener, F., Muntean, M., Pouliot, G., Keating, T., Zhang,
400 Q., Kurokawa, J., Wankmüller, R., Denier van der Gon, H., Kuenen, J. J. P., Klimont, Z., Frost, G.,
401 Darras, S., Koffi, B., and Li, M.: HTAP_v2.2: a mosaic of regional and global emission grid maps for
402 2008 and 2010 to study hemispheric transport of air pollution, *Atmos. Chem. Phys.*, 15, 11411–11432,
403 <https://doi.org/10.5194/acp-15-11411-2015>, 2015.



- 404 Ji, D., Cui, Y., Li, L., He, J., Wang, L., Zhang, H., Wang, W., Zhou, L., Maenhaut, W., Wen, T., and Wang, Y.:
405 Characterization and source identification of fine particulate matter in urban Beijing during the 2015
406 Spring Festival, *Sci. Total Environ.*, 628–629, 430–
407 440, <https://doi.org/10.1016/j.scitotenv.2018.01.304>, 2018.
- 408 Jiang, Z., Worden, J. R., Worden, H., Deeter, M., Jones, D. B. A., Arellano, A. F., and Henze, D. K.: A 15-year
409 record of CO emissions constrained by MOPITT CO observations, *Atmos. Chem. Phys.*, 17, 4565–
410 4583, <https://doi.org/10.5194/acp-17-4565-2017>, 2017.
- 411 Kalnay, E.: *Atmospheric modeling, data assimilation and predictability* (p. 341), Cambridge: Cambridge
412 University Press, 2002.
- 413 Kleist, D. T., Parrish, D. F., Derber, J. C., Treadon, R., Errico, R. M., and Yang, R.: Improving incremental
414 balance in the GSI 3DVAR analysis system, *Mon. Weather Rev.*, 137, 1046–1060,
415 doi:10.1175/2008MWR2623.1, 2009.
- 416 Le, T., Wang, Y., Liu, L., Yang, J., Yung, Y. L., Li, G., and Seinfeld, J. H.: Unexpected air pollution with marked
417 emission reductions during the COVID-19 outbreak in China, *Science*, 702–706,
418 <https://doi.org/10.1126/science.abb7431>, 2020.
- 419 Lei, Y., Zhang, Q., He, K. B., and Streets, D. G.: Primary anthropogenic aerosol emission trends for China,
420 1990–2005, *Atmos. Chem. Phys.*, 11, 931–954, <https://doi.org/10.5194/acp-11-931-2011>, 2011.
- 421 Li, N., Tang, K., Wang, Y., Wang, J., Feng, W., Zhang, H., Liao, H., Hu, J., Long, X., and Shi, C.: Is the efficacy
422 of satellite-based inversion of SO₂ emission model dependent? *Environmental Research Letters*, 16,
423 035018, 2021.
- 424 Li, K., Jacob, D. J., Liao, H., Zhu, J., Shah, V., Shen, L., Bates, K. H., Zhang, Q., and Zhai, S.: A Two-Pollutant
425 Strategy for Improving Ozone and Particulate Air Quality in China, *Nat. Geosci.*, 12, 906–
426 910, <https://doi.org/10.1038/s41561-019-0464-x>, 2019a.
- 427 Li, J. and Wang, Y.: Inferring the anthropogenic NO_x emission trend over the United States during 2003–2017
428 from satellite observations: was there a flattening of the emission trend after the Great Recession?
429 *Atmos. Chem. Phys.*, 19, 15339–15352, <https://doi.org/10.5194/acp-19-15339-2019>, 2019b.
- 430 Li, M., Zhang, Q., Kurokawa, J.-I., Woo, J.-H., He, K., Lu, Z., Ohara, T., Song, Y., Streets, D. G., Carmichael,
431 G. R., Cheng, Y., Hong, C., Huo, H., Jiang, X., Kang, S., Liu, F., Su, H., and Zheng, B.: MIX: a mosaic
432 Asian anthropogenic emission inventory under the international collaboration framework of the MICS-
433 Asia and HTAP, *Atmos. Chem. Phys.*, 17, 935–963, <https://doi.org/10.5194/acp-17-935-2017>, 2017.
- 434 Li, M., Zhang, Q., Streets, D. G., He, K. B., Cheng, Y. F., Emmons, L. K., Huo, H., Kang, S. C., Lu, Z., Shao,
435 M., Su, H., Yu, X., and Zhang, Y.: Mapping Asian anthropogenic emissions of non-methane volatile
436 organic compounds to multiple chemical mechanisms, *Atmos. Chem. Phys.*, 14, 5617–
437 5638, <https://doi.org/10.5194/acp-14-5617-2014>, 2014.



- 438 Liu, J., Yin, H., Tang, X., Zhu, T., Zhang, Q., Liu, Z., Tang, X., and Yi, H.: Transition in air pollution, disease
439 burden and health cost in China: A comparative study of long-term and short-term exposure,
440 *Environmental Pollution*, 277, 116770, 2021.
- 441 Liu, T., Wang, X. Y., Hu, J. L., Wang, Q., An, J. Y., Gong, K. J., Sun, J. J., Li, L., Qin, M. M., Li, J. Y.,
442 Tian, J. J., Huang, Y. W., Liao, H., Zhou, M., Hu, Q. Y., Yan, R. S., Wang, H. L., and Huang, C.:
443 Driving Forces of Changes in Air Quality during the COVID-19 Lockdown Period in the Yangtze River
444 Delta Region, China, *Environ. Sci. Technol.*, 7, 779–786, <https://doi.org/10.1021/acs.estlett.0c00511>,
445 2020.
- 446 Liu, T., Cai, Y., Feng, B., Cao, G., Lin, H., Xiao, J., Li, X., Liu, S., Pei, L., Fu, L., Yang, X., and Zhang, B.:
447 Long-term mortality benefits of air quality improvement during the twelfth five-year-plan period in 31
448 provincial capital cities of China, *Atmospheric Environment*, 173, 53–61,
449 <https://doi.org/10.1016/j.atmosenv.2017.10.054>, 2018.
- 450 Liu, Z., Liu, Q., Lin, H. C., Schwartz, C. S., Lee, Y. H., and Wang, T.: Three-dimensional variational
451 assimilation of MODISAerosol optical depth: implementation and application to a dust storm over
452 East Asia, *J. Geophys. Res.*, 116, D23206, <https://doi.org/10.1029/2011JD016159>, 2011.
- 453 Miyazaki, K., Bowman, K., Sekiya, T., Eskes, H., Boersma, F., Worden, H., Livesey, N., Payne, V. H., Sudo,
454 K., Kanaya, Y., Takigawa, M., and Ogochi, K.: Updated tropospheric chemistry reanalysis and emission
455 estimates, TCR-2, for 2005–2018, *Earth Syst. Sci. Data*, 12, 2223–2259, [https://doi.org/10.5194/essd-](https://doi.org/10.5194/essd-12-2223-2020)
456 [12-2223-2020](https://doi.org/10.5194/essd-12-2223-2020), 2020.
- 457 Miyazaki, K., Eskes, H., Sudo, K., Boersma, K. F., Bowman, K., and Kanaya, Y.: Decadal changes in global
458 surface NO_x emissions from multi-constituent satellite data assimilation, *Atmos. Chem. Phys.*, 17, 807–
459 837, <https://doi.org/10.5194/acp-17-807-2017>, 2017.
- 460 Müller, J.-F., Stavrou, T., Bauwens, M., George, M., Hurtmans, D., Coheur, P.-F., Clerbaux, C., and Sweeney,
461 C.: Top-Down CO Emissions Based on IASI Observations and Hemispheric Constraints on OH Levels,
462 *Geophys. Res. Lett.*, 45, 1621–1629, <https://doi.org/10.1002/2017GL076697>, 2018.
- 463 Notice of the State Council on Adjusting the Standards for Categorizing City Sizes (in Chinese) (Chinese State
464 Council, 2014); http://www.gov.cn/zwqk/2013-09/12/content_2486773.htm
- 465 Peng, Z., Lei, L., Liu, Z., Liu, H., Chu, K., and Kou, X.: Impact of Assimilating Meteorological Observations
466 on Source Emissions Estimate and Chemical Simulations, *Geophys. Res. Lett.*, 47,
467 e2020GL089030, <https://doi.org/10.1029/2020GL089030>, 2020.
- 468 Peng, Z., Lei, L., Liu, Z., Sun, J., Ding, A., Ban, J., Chen, D., Kou, X., and Chu, K.: The impact of multi-species
469 surface chemical observation assimilation on air quality forecasts in China, *Atmos. Chem. Phys.*, 18,
470 17387–17404, <https://doi.org/10.5194/acp-18-17387-2018>, 2018.
- 471 Peng, Z., Liu, Z., Chen, D., and Ban, J.: Improving PM_{2.5} forecast over China by the joint adjustment of initial
472 conditions and source emissions with an ensemble Kalman filter, *Atmos. Chem. Phys.*, 17, 4837–
473 4855, <https://doi.org/10.5194/acp-17-4837-2017>, 2017.



- 474 Peng, Z., Zhang, M., Kou, X., Tian, X., and Ma, X.: A regional carbon data assimilation system and its
475 preliminary evaluation in East Asia, *Atmos. Chem. Phys.*, 15, 1087–1104, [https://doi.org/10.5194/acp-](https://doi.org/10.5194/acp-15-1087-2015)
476 [15-1087-2015](https://doi.org/10.5194/acp-15-1087-2015), 2015.
- 477 Peters, W., Jacobson, A. R., Sweeney, C., Andrews, A. E., Conway, T. J., Masarie, K., Miller, J. B., Bruhwiler,
478 L. M. P., Petron, G., Hirsch, A. I., Worthy, D. E. J., van der Werf, G. R., Randerson, J. T., Wennberg, P.
479 O., Krol, M. C., and Tans, P. P.: An atmospheric perspective on North American carbon dioxide
480 exchange: CarbonTracker, *P. Natl. Acad. Sci. USA*, 104, 18925–18930, 2007.
- 481 Qu, Z., Henze, D. K., Capps, S. L., Wang, Y., Xu, X., and Wang, J.: Monthly top-down NO_x emissions for
482 China (2005–2012): a hybrid inversion method and trend analysis, *J. Geophys. Res.*, 122, 4600–4625,
483 <https://doi.org/10.1002/2016JD025852>, 2017.
- 484 Streets, D. G., Bond, T. M. L., Carmichael, G. R., Fernandes, S., Fu, Q., He, D., Klimont, Z., Nelson, S. M.,
485 Tsai, N. Y., Wang, M. Q., Woo, J.-H., and Yarber, K. F.: An inventory of gaseous and primary aerosol
486 emissions in Asia in the year 2000. *J. Geophys. Res.*, 108(D21), 8809, doi:10.1029/2002JD003093,
487 2003.
- 488 Torn, R. D., Hakim, G. J., and Snyder, C.: Boundary conditions for limited-area ensemble Kalman filters, *Mon.*
489 *Weather Rev.*, 134, 2490–2502, 2006.
- 490 Wang, H., He, X., Liang, X., Choma, E. F., Liu, Y., Shan, L., Zheng, H., Zhang, S., Nielsen, C. P., Wang, S.,
491 Wu, Y., and Evans, J. S.: Health benefits of on-road transportation pollution control programs in China,
492 *P. Natl. Acad. Sci. USA*, 117, 25370, <https://doi.org/10.1073/pnas.1921271117>, 2020.
- 493 Wang, G., Cheng, S. Y., Wei, W., Yang, X. W., Wang, X. Q., Jia, J., Lang, J. L., and Lv, Z.: Characteristics and
494 emission reduction measures evaluation of PM_{2.5} during the two major events: APEC and Parade, *Sci.*
495 *Total Environ.*, 595, 81–92, <https://doi.org/10.1016/j.scitotenv.2017.03.231>, 2017.
- 496 Wang, Z., Li, J., Wang, Z., Yang, W., Tang, X., Ge, B., Yan, P., Zhu, L., Chen, X., and Chen, H.: Modeling study
497 of regional severe hazes over mid-eastern China in January 2013 and its implications on pollution
498 prevention and control, *Sci. China-Earth Sci.*, 57, 3–13, 2014.
- 499 Wang, X. Y., Liang, X. Z., Jiang, W. M., Tao, Z. N., Wang, J. X. L., Liu, H. N., Han, Z. W., Liu, S. Y., Zhang, Y. Y.,
500 Grell, G. A., and Peckham, S. E.: WRF-Chem simulation of East Asian air quality: Sensitivity to temporal
501 and vertical emissions distributions, *Atmos. Environ.*, 44, 660–669, 2010.
- 502 Whitaker, J. S. and Hamill, T. M.: Ensemble data assimilation without perturbed observations, *Mon. Weather Rev.*,
503 130, 1913–1924, 2002.
- 504 Whitaker, J. S. and Hamill, T. M.: Evaluating methods to account for system errors in ensemble data assimilation,
505 *Mon. Weather Rev.*, 140, 3078–3089, 2012.
- 506 Yang, Y., Ren, L., Li, H., Wang, H., Wang, P., Chen, L., Yue, X., and Liao, H.: Fast climate responses to aerosol
507 emission reductions during the COVID-19 pandemic, *Geophys. Res. Lett.*, 47,
508 e2020GL089788, <https://doi.org/10.1029/2020gl089788>, 2020.



- 509 Zhai, S., Jacob, D. J., Wang, X., Liu, Z., Wen, T., Shah, V., Li, K., Moch, J. M., Bates, K. H., Song, S., Shen,
510 L., Zhang, Y., Luo, G., Yu, F., Sun, Y., Wang, L., Qi, M., Tao, J., Gui, K., Xu, H., Zhang, Q., Zhao, T.,
511 Wang, Y., Lee, H. C., Choi, H., and Liao, H.: Control of particulate nitrate air pollution in China, *Nat.*
512 *Geosci.*, 14, 1–7, 2021.
- 513 Zhang, Q., Zheng, Y., Tong, D., Shao, M., Wang, S., Zhang, Y., Xu, X., Wang, J., He, H., Liu, W., Ding, Y.,
514 Lei, Y., Li, J., Wang, Z., Zhang, X., Wang, Y., Cheng, J., Liu, Y., Shi, Q., Yan, L., Geng, G., Hong, C.,
515 Li, M., Liu, F., Zheng, B., Cao, J., Ding, A., Gao, J., Fu, Q., Huo, J., Liu, B., Liu, Z., Yang, F., He, K.,
516 and Hao, J.: Drivers of Improved PM_{2.5} Air Quality in China from 2013 to 2017, *P. Natl. Acad. Sci.*
517 *USA*, 116, 24463–24469, <https://doi.org/10.1073/pnas.1907956116>, 2019.
- 518 Zhang, L., Shao, J. Y., Lu, X., Zhao, Y. H., Hu, Y. Y., Henze, D. K., Liao, H., Gong, S., and Zhang, Q.: Sources
519 and processes affect-ing fine particulate matter pollution over North China: An adjoint analysis of the
520 Beijing APEC period, *Environ. Sci. Technol.*, 50, 8731–8740, <https://doi.org/10.1021/acs.est.6b03010>,
521 2016.
- 522 Zhang, Q., Streets, D. G., Carmichael, G. R., He, K. B., Huo, H., Kannari, A., Klimont, Z., Park, I. S., Reddy,
523 S., Fu, J. S., Chen, D., Duan, L., Lei, Y., Wang, L. T., and Yao, Z. L.: Asian emis- sions in 2006 for the
524 NASA INTEX-B mission, *Atmos. Chem. Phys.*, 9, 5131–5153, [https://doi.org/10.5194/acp-9-5131-](https://doi.org/10.5194/acp-9-5131-2009)
525 [2009](https://doi.org/10.5194/acp-9-5131-2009), 2009.
- 526 Zheng, B., Zhang, Q., Geng, G., Chen, C., Shi, Q., Cui, M., Lei, Y., and He, K.: Changes in China's
527 anthropogenic emissions and air quality during the COVID-19 pandemic in 2020, *Earth Syst. Sci. Data*,
528 13, 2895–2907, <https://doi.org/10.5194/essd-13-2895-2021>, 2021.
- 529 Zheng, B., Geng, G., Ciais, P., Davis, S. J., Martin, R. V., Meng, J., Wu, N., Chevallier, F., Broquet, G.,
530 Boersma, F., van der A, R., Lin, J., Guan, D., Lei, Y., He, K., and Zhang, Q.: Satellite-based estimates
531 of decline and rebound in China's CO₂ emissions during COVID-19 pandemic, *Sci. Adv.*, 6,
532 eabd4998, <https://doi.org/10.1126/sciadv.abd4998>, 2020.
- 533 Zheng, B., Tong, D., Li, M., Liu, F., Hong, C., Geng, G., Li, H., Li, X., Peng, L., Qi, J., Yan, L., Zhang, Y.,
534 Zhao, H., Zheng, Y., He, K., and Zhang, Q.: Trends in China's anthropogenic emissions since 2010 as
535 the consequence of clean air actions, *Atmos. Chem. Phys.*, 18, 14095–14111,
536 <https://doi.org/10.5194/acp-18-14095-2018>, 2018.
- 537 Zhu, J., Chen, L., Liao, H., Yang, H., Yang, Y., and Yue, X.: Enhanced PM_{2.5} Decreases and O₃ Increases in
538 China during COVID-19 Lockdown by Aerosol-Radiation Feedback, *Geophys. Res. Lett.*, 48,
539 e2020GL090260, <https://doi.org/10.1029/2020GL090260>, 2021.

540
541

542 **Figures and Tables**

543 **Captions:**



544 **Figure 1.** Times series of hourly $\text{PM}_{2.5}$ concentration biases ($\mu\text{g}\cdot\text{m}^{-3}$). The ensemble mean priors
545 compared to the observed quantities for December of years 2016-2020 (gray and black), and the
546 mean biases of years 2016-2020 (blue).

547 **Figure 2.** Model domain and observation sites for cycling assimilation. Red and blue dots denote
548 the assimilated and unassimilated observational sites, respectively.

549 **Figure 3.** (a) Dynamics-based monthly $\text{PM}_{2.5}$ emission estimates ($\text{Tg}\cdot\text{day}^{-1}$) summed over
550 mainland China of each year from 2016 to 2020 (colored) and the estimated $\text{PM}_{2.5}$ emission from
551 MEIC (gray); (b) Ratio of $\text{PM}_{2.5}$ emission changes between two adjacent years from year 2016 to
552 2020 normalized by the $\text{PM}_{2.5}$ emission of year 2016; (c) Monthly fractions of dynamics-based
553 $\text{PM}_{2.5}$ emission estimates for years 2016-2020 (light blue), the five-year mean fractions of
554 dynamics-based monthly $\text{PM}_{2.5}$ emission estimates with bars denoting one standard deviation of
555 the five-year variations (dark blue), and the monthly fractions of estimated $\text{PM}_{2.5}$ emission from
556 MEIC (gray).

557 **Figure 4.** (a) Spatial distribution of dynamics-based $\text{PM}_{2.5}$ emission estimates ($\mu\text{g}\cdot\text{m}^{-2}\cdot\text{s}^{-1}$) for
558 year 2016, and compared to that of year 2016, spatial distributions of dynamics-based $\text{PM}_{2.5}$
559 emission changes of year (b) 2017, (c) 2018, (d) 2019 and (e) 2020.

560 **Figure 5.** (a) The differences of dynamics-based $\text{PM}_{2.5}$ emission estimates between years 2017-
561 2020 and 2016, and (b) the differences normalized by that of year 2016.

562 **Figure 6.** Five-year mean diurnal variations of dynamics-based $\text{PM}_{2.5}$ emission fraction averaged
563 over (a) mainland China, (b) megacities with urban population ≥ 5 million, and (c) non-megacities
564 with urban population < 5 million.

565 **Figure 7.** Diurnal variations of dynamics-based $\text{PM}_{2.5}$ emission fractions for years 2016-2020
566 (light blue) and five-year mean fractions with bars denoting one standard deviation of the five-
567 year variations (dark blue) are averaged over mainland China for (a) January, (b) April, (c) July,
568 and (d) October.

569 **Figure 8.** Diurnal variations of $\text{PM}_{2.5}$ emission fraction for each month based on diurnal variation
570 profiles from ES and EU (Wang et al. 2010).

571 **Figure 9.** Hourly (light red and blue) and daily (dark red and blue) dynamics-based $\text{PM}_{2.5}$ emission
572 estimates ($\text{kg}\cdot\text{h}^{-1}$) summed over mainland China from January to March of years 2019 and 2020.



573 **Figure 10.** Spatial distributions of dynamics-based $\text{PM}_{2.5}$ emission estimates ($\mu\text{g}\cdot\text{m}^{-2}\cdot\text{s}^{-1}$) on (b)
574 February and (d) March of year 2019, and spatial distributions of dynamics-based $\text{PM}_{2.5}$ emission
575 reduction of year 2020 compared to year 2019 for (c) February and (e) March.

576 **Figure 11.** Mean spatial distributions of $\text{PM}_{2.5}$ emission differences ($\mu\text{g}\cdot\text{m}^{-2}\cdot\text{s}^{-1}$) between year
577 2020 and 2019 for 9 weeks starting at 9 January 2020. Negative (positive) values indicate that
578 $\text{PM}_{2.5}$ emission of year 2020 is smaller (larger) than that of year 2019. The numbers in (a) denote
579 provinces as: 1 Heilongjiang, 2 Neimenggu, 3 Xinjiang, 4 Jilin, 5 Liaoning, 6 Gansu, 7 Hebei, 8
580 Beijing, 9 Shanxi, 10 Tianjin, 11 Shanxi, 12 Ningxia, 13 Qinghai, 14 Shandong, 15 Xizang, 16
581 Henan, 17 Jiangsu, 18 Anhui, 19 Sichuan, 20 Hubei, 21 Chongqing, 22 Shanghai, 23 Zhejiang, 24
582 Hunan, 25 Jiangxi, 26 Yunnan, 27 Guizhou, 28 Fujian, 29 Guangxi, 30 Guangdong, 31 Taiwan,
583 32 Hongkong, 33 Macao, 34 Hainan.

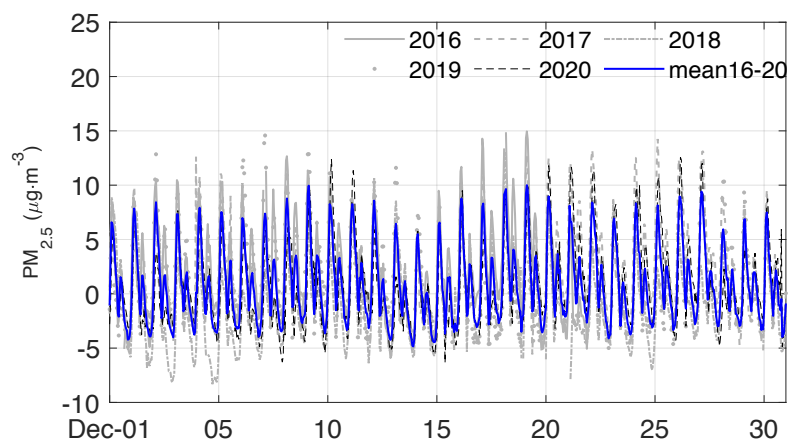
584 **Table 1.** Dynamics-based $\text{PM}_{2.5}$ emission estimates of year 2016 for each province whose value
585 is larger than $0.01 \mu\text{g}\cdot\text{m}^{-2}\cdot\text{s}^{-1}$ are shown in the second column. Ratios of $\text{PM}_{2.5}$ emission changes
586 of years 2017-2020 compared to year 2016 are shown from the third to the sixth column, with
587 negative (positive) values indicating decrease (increase) of $\text{PM}_{2.5}$ emission.

588 **Table 2.** Five-year mean diurnal fractions (%) of the dynamics-based $\text{PM}_{2.5}$ emission estimates
589 over mainland China on local solar time (LST) for each month.

590



591
592

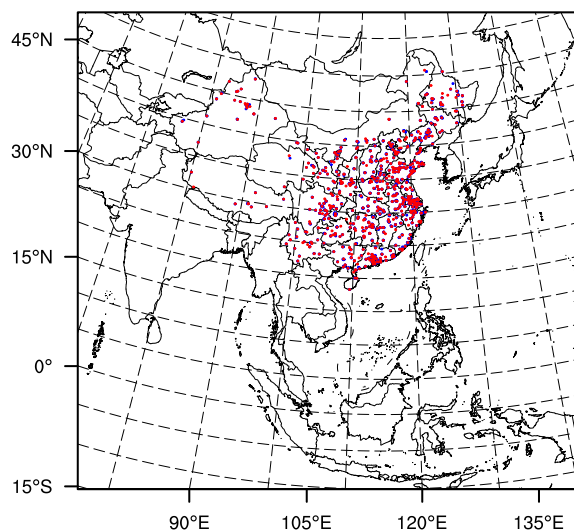


593
594
595
596
597
598
599

Figure 1. Times series of hourly $PM_{2.5}$ concentration biases ($\mu\text{g}\cdot\text{m}^{-3}$). The ensemble mean priors compared to the observed quantities for December of years 2016-2020 (gray and black), and the mean biases of years 2016-2020 (blue).

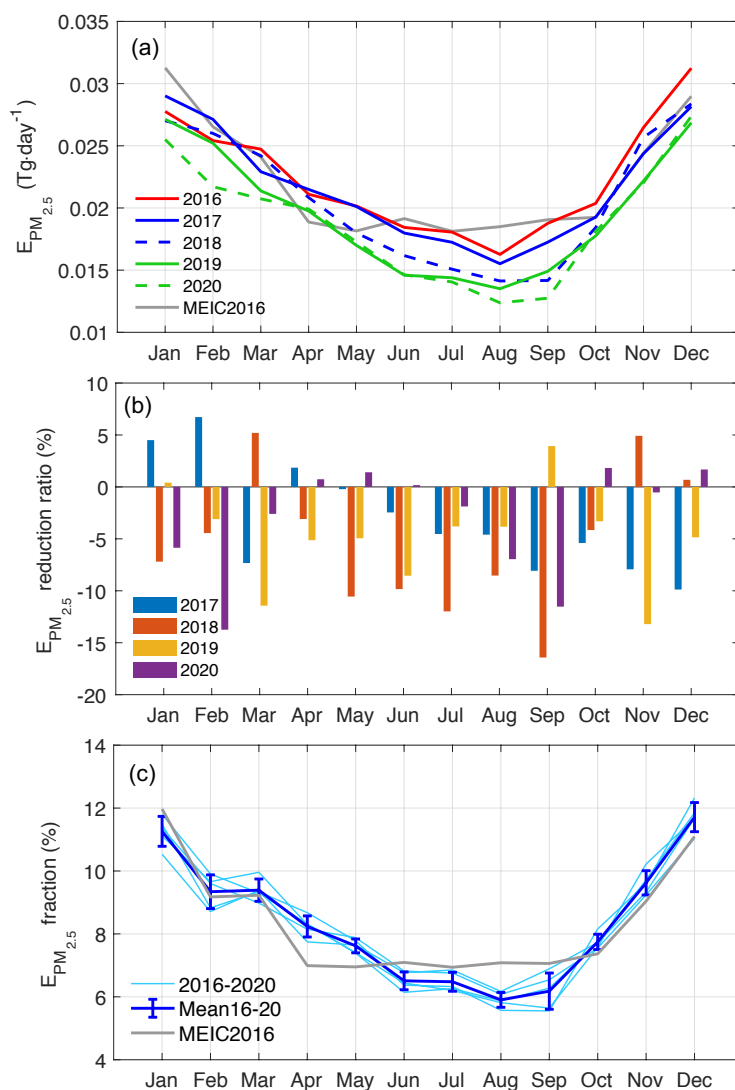


600



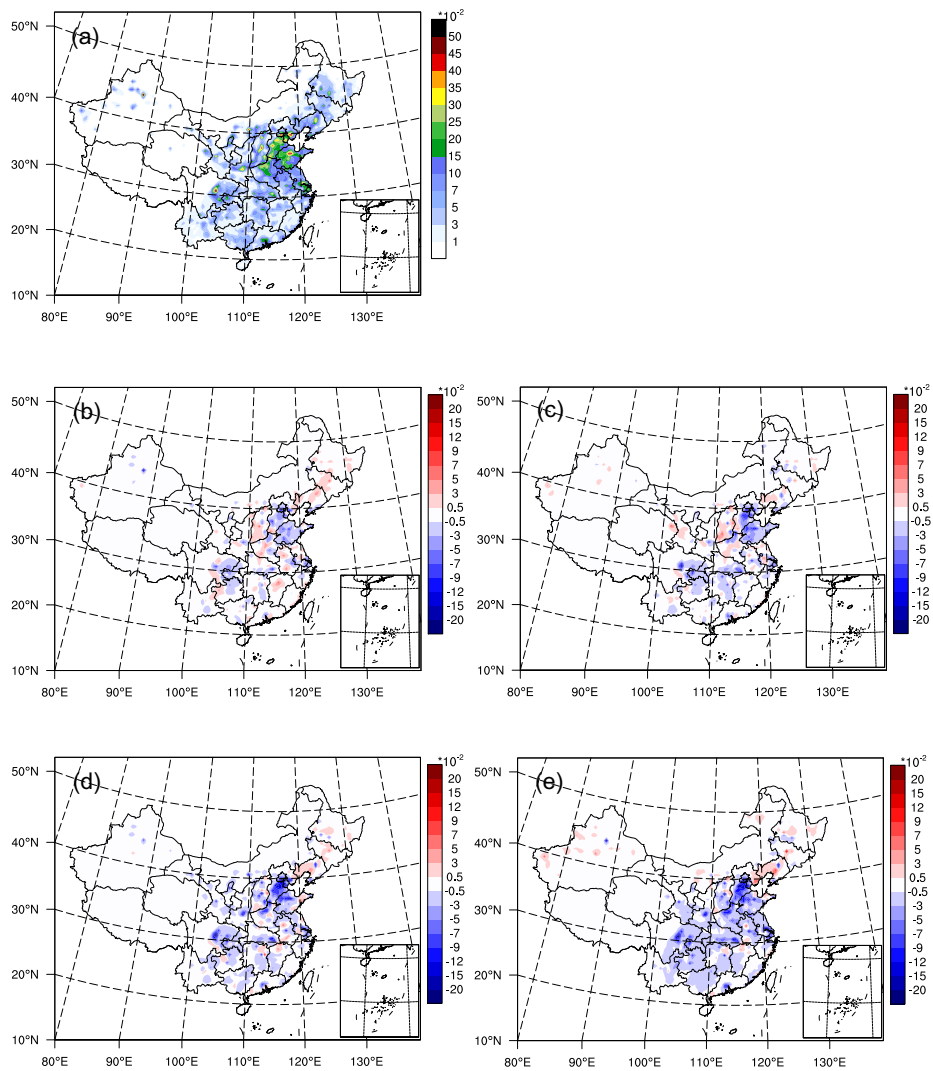
601
602
603
604
605

Figure 2. Model domain and observation sites for cycling assimilation. Red and blue dots denote the assimilated and unassimilated observational sites, respectively.



606
607
608
609
610
611
612
613
614
615

Figure 3. (a) Dynamics-based monthly PM_{2.5} emission estimates (Tg·day⁻¹) summed over mainland China of each year from 2016 to 2020 (colored) and the estimated PM_{2.5} emission from MEIC (gray); (b) Ratio of PM_{2.5} emission changes between two adjacent years from year 2016 to 2020 normalized by the PM_{2.5} emission of year 2016; (c) Monthly fractions of dynamics-based PM_{2.5} emission estimates for years 2016-2020 (light blue), the five-year mean fractions of dynamics-based monthly PM_{2.5} emission estimates with bars denoting one standard deviation of the five-year variations (dark blue), and the monthly fractions of estimated PM_{2.5} emission from MEIC (gray).



616

617 **Figure 4.** (a) Spatial distribution of dynamics-based $PM_{2.5}$ emission estimates ($\mu g \cdot m^{-2} \cdot s^{-1}$) for year 2016, and
618 compared to that of year 2016, spatial distributions of dynamics-based $PM_{2.5}$ emission changes of year (b)

619 2017, (c) 2018, (d) 2019 and (e) 2020.

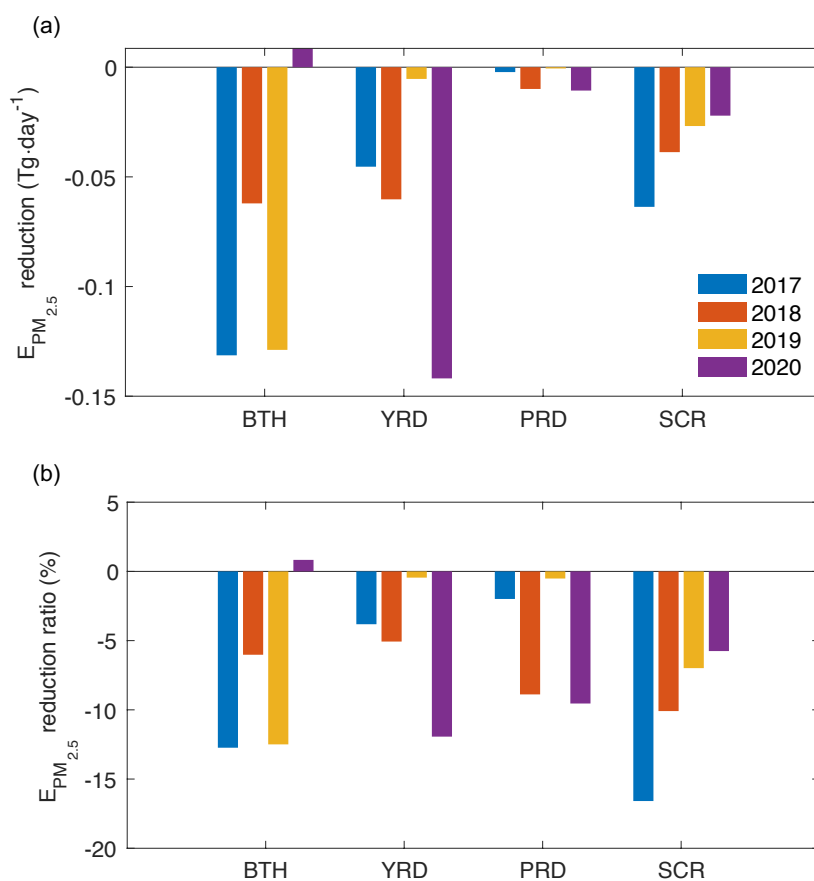
620

621

622



623



624

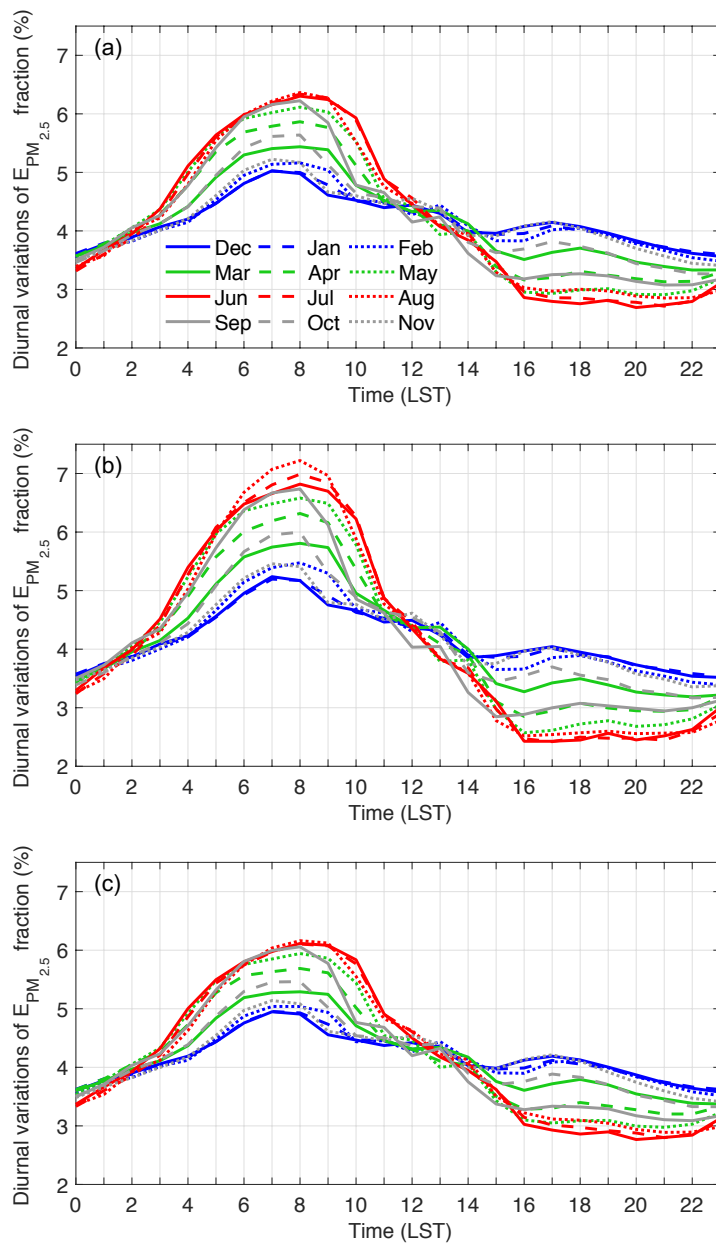
625

626

627

628

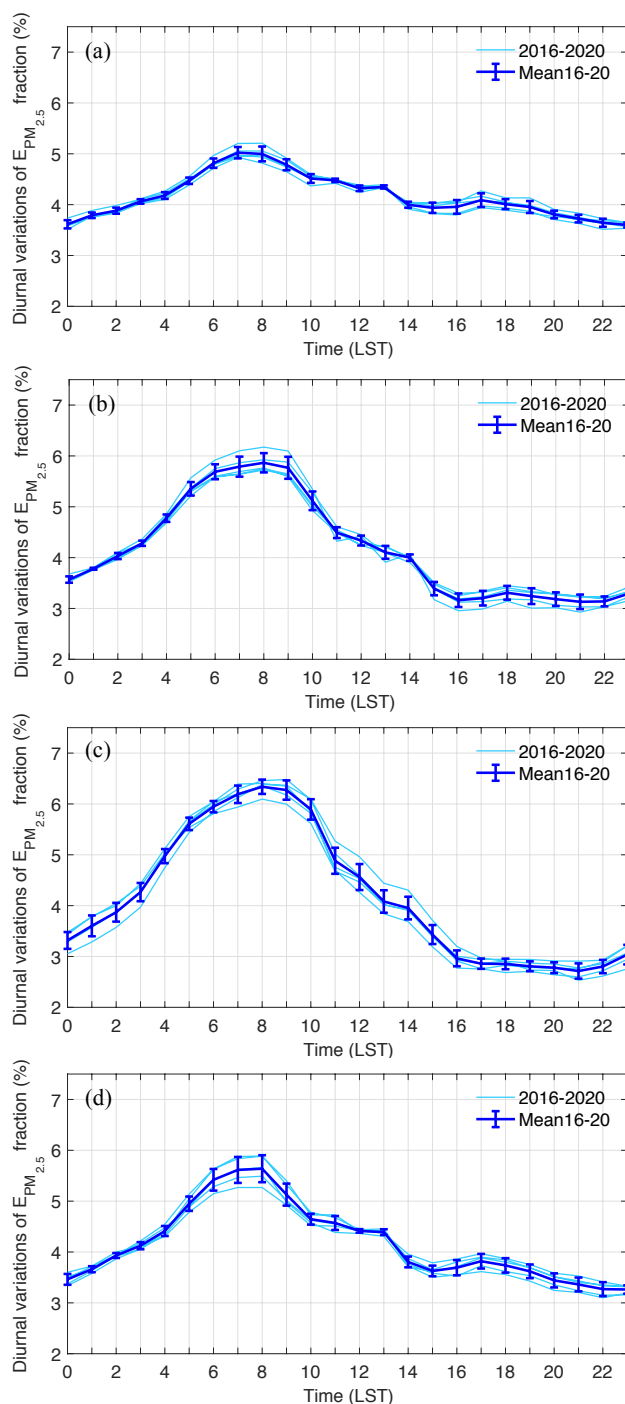
Figure 5. (a) The differences of dynamics-based PM_{2.5} emission estimates between years 2017-2020 and 2016, and (b) the differences normalized by that of year 2016.



629

630 **Figure 6.** Five-year mean diurnal variations of dynamics-based $PM_{2.5}$ emission fraction averaged over (a) mainland

631 China, (b) megacities with urban population ≥ 5 million, and (c) non-megacities with urban population < 5 million.



632

633

634

Figure 7. Diurnal variations of dynamics-based $PM_{2.5}$ emission fractions for years 2016-2020 (light blue) and five-year mean fractions with bars denoting one standard deviation of the five-

<https://doi.org/10.5194/egusphere-2023-755>

Preprint. Discussion started: 28 April 2023

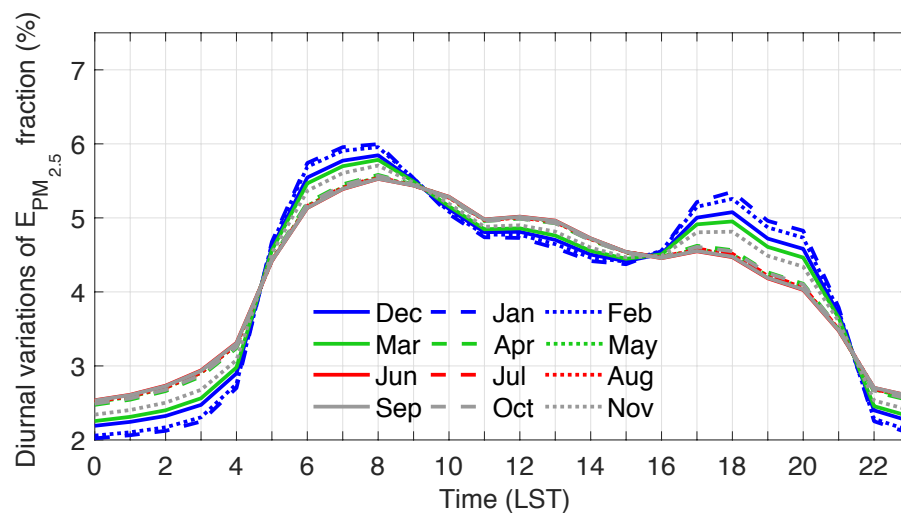
© Author(s) 2023. CC BY 4.0 License.



635 year variations (dark blue) are averaged over mainland China for (a) January, (b) April, (c) July,
636 and (d) October.
637



638
639



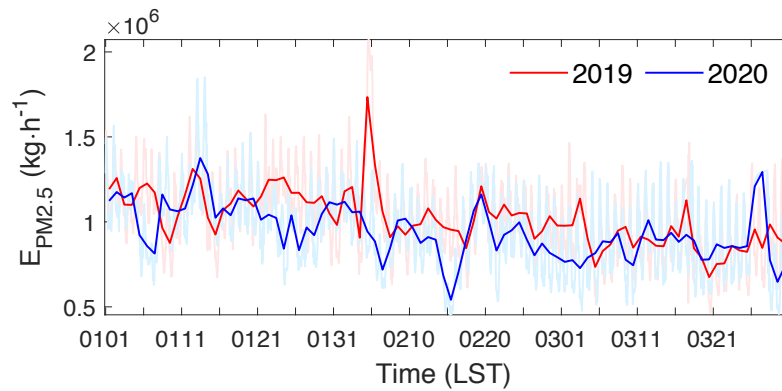
640
641
642
643

Figure 8. Diurnal variations of $PM_{2.5}$ emission fraction for each month based on diurnal variation profiles from ES and EU (Wang et al. 2010).



644

645



646

647

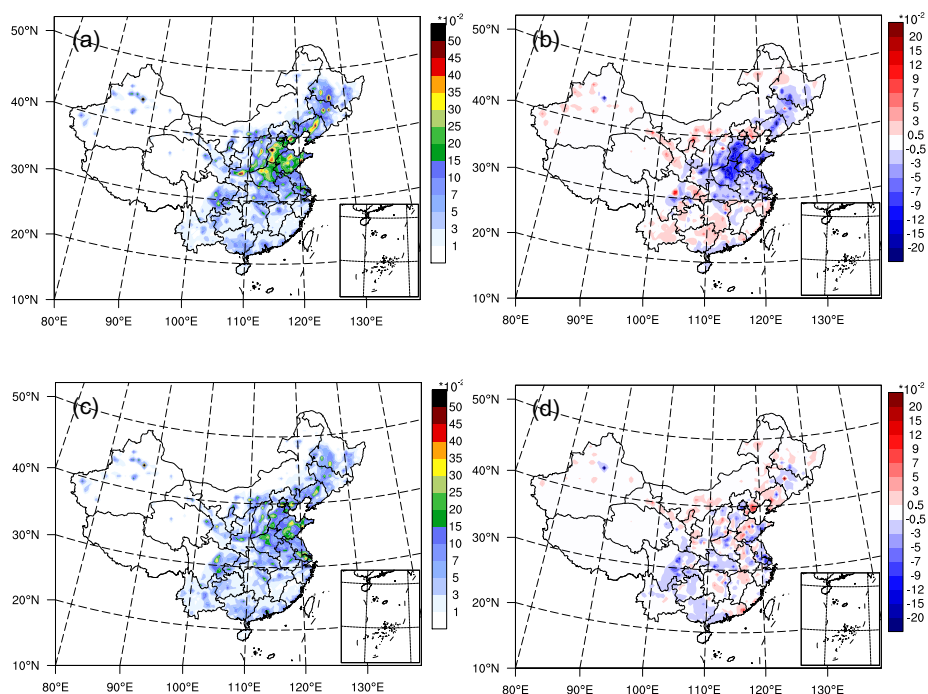
648

649

Figure 9. Hourly (light red and blue) and daily (dark red and blue) dynamics-based PM_{2.5} emission estimates (kg·h⁻¹ summed over mainland China from January to March of years 2019 and 2020.



650



651

652

653 **Figure 10.** Spatial distributions of dynamics-based PM_{2.5} emission estimates ($\mu\text{g}\cdot\text{m}^{-2}\cdot\text{s}^{-1}$) on (b) February and (d)

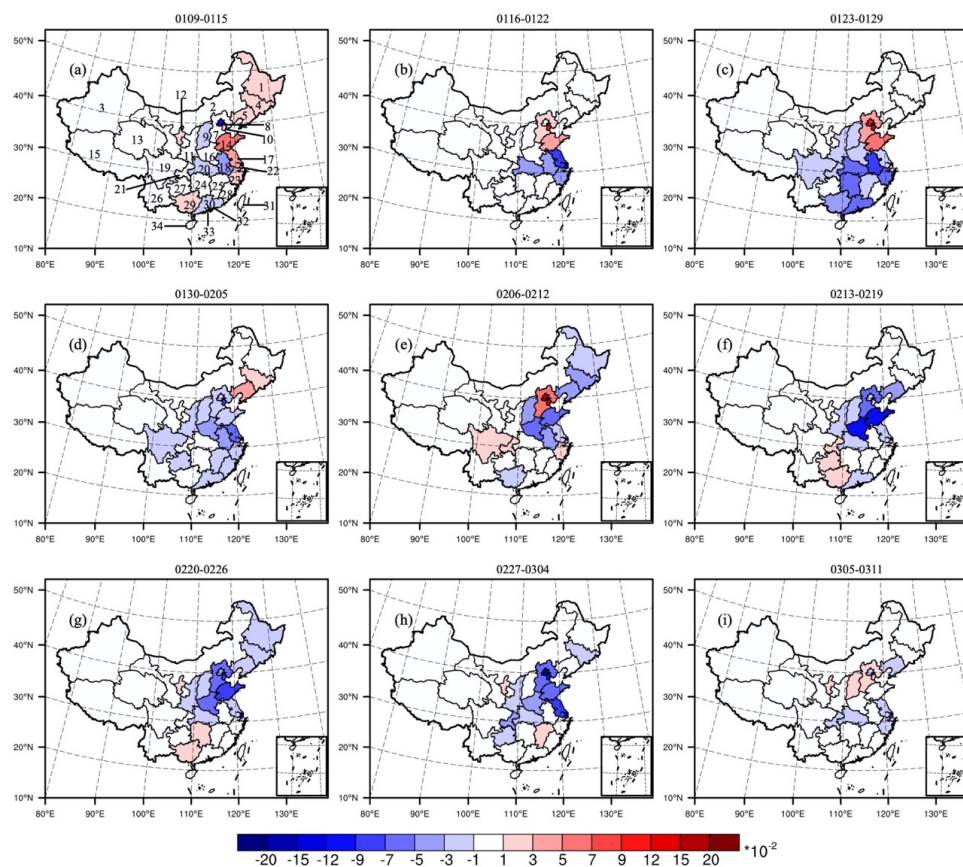
654 March of year 2019, and spatial distributions of dynamics-based PM_{2.5} emission reduction of year 2020 compared to

655 year 2019 for (c) February and (e) March.

656



657



658 **Figure 11.** Mean spatial distributions of PM_{2.5} emission differences ($\mu\text{g}\cdot\text{m}^{-2}\cdot\text{s}^{-1}$) between year
 659 2020 and 2019 for 9 weeks starting at 9 January 2020. Negative (positive) values indicate that
 660 PM_{2.5} emission of year 2020 is smaller (larger) than that of year 2019. The numbers in (a) denote
 661 provinces as: 1 Heilongjiang, 2 Neimenggu, 3 Xinjiang, 4 Jilin, 5 Liaoning, 6 Gansu, 7 Hebei, 8
 662 Beijing, 9 Shanxi, 10 Tianjin, 11 Shanxi, 12 Ningxia, 13 Qinghai, 14 Shandong, 15 Xizang, 16
 663 Henan, 17 Jiangsu, 18 Anhui, 19 Sichuan, 20 Hubei, 21 Chongqing, 22 Shanghai, 23 Zhejiang,
 664 24 Hunan, 25 Jiangxi, 26 Yunnan, 27 Guizhou, 28 Fujian, 29 Guangxi, 30 Guangdong, 31
 665 Taiwan, 32 Hongkong, 33 Macao, 34 Hainan.

666

667



668 **Table 1.** Dynamics-based PM_{2.5} emission estimates of year 2016 for each province whose value
 669 is larger than 0.01 μg·m⁻²·s⁻¹ are shown in the second column. Ratios of PM_{2.5} emission changes
 670 of years 2017-2020 compared to year 2016 are shown from the third to the sixth column, with
 671 negative (positive) values indicating decrease (increase) of PM_{2.5} emission.
 672

Province	PM _{2.5} emission of year 2016 (μg·m ⁻² ·s ⁻¹)	Percentage of PM _{2.5} emission change for year 2017 (%)	Percentage of PM _{2.5} emission change for year 2018 (%)	Percentage of PM _{2.5} emission change for year 2019 (%)	Percentage of PM _{2.5} emission change for year 2020 (%)
Tianjin	0.2083	-14.07	-22.99	-38.70	-26.98
Shanghai	0.2067	-24.39	-30.21	-21.46	-30.05
Shandong	0.1631	-15.26	-21.02	-15.57	-19.41
Beijing	0.1598	-26.64	-25.75	-41.92	-45.27
Hebei	0.1178	-7.47	-11.98	-26.39	-22.87
Jiangsu	0.1088	-6.52	-3.98	-12.69	-28.20
Henan	0.1064	-1.41	-3.68	-12.15	-24.91
Shanxi	0.0885	<u>6.17</u>	<u>7.90</u>	-13.18	-13.85
Liaoning	0.0742	<u>6.32</u>	-2.58	<u>3.22</u>	<u>11.42</u>
Anhui	0.0687	<u>1.92</u>	-5.63	-6.23	-21.57
Hubei	0.0574	-5.87	-17.69	-19.76	-36.48
Zhejiang	0.0557	-3.62	-9.32	-9.99	-18.05
Chongqing	0.0525	-22.24	-29.81	-24.63	-38.41
Shanxi	0.0498	<u>0.62</u>	-1.97	-18.05	-17.85
Guangdong	0.0481	<u>1.21</u>	-6.01	-6.69	-14.37
Ningxia	0.0481	-8.17	-5.93	-24.46	-12.95
Hunan	0.0417	-6.40	-19.35	-9.91	-20.62
Guangxi	0.0390	-2.42	-3.52	-12.47	-22.31
Guizhou	0.0365	-4.01	-15.82	-21.74	-46.41
Jilin	0.0360	<u>12.30</u>	-3.22	<u>7.37</u>	<u>4.76</u>
Jiangxi	0.0353	<u>13.22</u>	-9.67	-7.19	-11.91
Sichuan	0.0337	-7.66	-15.66	-27.68	-37.93
Fujian	0.0244	<u>3.13</u>	-2.73	-8.13	-13.41
Heilongjiang	0.0231	<u>7.30</u>	-0.21	<u>3.14</u>	<u>3.91</u>
Yunnan	0.0221	-1.26	-7.16	-9.93	-15.35
Gansu	0.0177	-4.26	<u>5.28</u>	-17.89	-16.49
Hainan	0.0173	<u>3.93</u>	-0.41	-5.04	-4.78
Neimenggu	0.0141	-0.00	-3.63	-8.16	<u>3.55</u>

673
674



675 **Table 2.** Five-year mean diurnal fractions (%) of the dynamics-based PM_{2.5} emission estimates
 676 over mainland China on local solar time (LST) for each month.

	Jan	Feb	Mar	Apr	May	Jun	Jul	Aug	Sep	Oct	Nov	Dec
0	3.61	3.53	3.57	3.57	3.50	3.36	3.33	3.39	3.51	3.46	3.49	3.59
1	3.79	3.71	3.74	3.78	3.76	3.67	3.60	3.58	3.72	3.66	3.66	3.77
2	3.88	3.82	3.97	4.03	4.05	3.95	3.87	4.01	4.05	3.93	3.83	3.89
3	4.06	4.02	4.12	4.28	4.37	4.37	4.27	4.22	4.26	4.12	4.01	4.07
4	4.18	4.15	4.42	4.78	5.01	5.11	4.97	4.80	4.77	4.41	4.21	4.20
5	4.47	4.53	4.92	5.35	5.61	5.64	5.61	5.55	5.42	4.95	4.60	4.47
6	4.82	4.95	5.30	5.69	5.92	5.98	5.95	5.98	5.95	5.42	5.04	4.81
7	5.02	5.14	5.41	5.79	6.02	6.16	6.19	6.22	6.16	5.61	5.22	5.03
8	5.00	5.16	5.44	5.87	6.12	6.30	6.34	6.36	6.22	5.64	5.17	4.98
9	4.78	5.04	5.39	5.77	6.03	6.24	6.27	6.27	5.85	5.13	4.66	4.61
10	4.51	4.51	4.78	5.12	5.53	5.93	5.89	5.52	4.78	4.66	4.60	4.52
11	4.48	4.50	4.52	4.49	4.55	4.89	4.88	4.76	4.66	4.57	4.46	4.40
12	4.32	4.28	4.33	4.34	4.43	4.45	4.56	4.47	4.15	4.42	4.56	4.44
13	4.35	4.44	4.35	4.10	3.94	4.07	4.08	4.10	4.24	4.39	4.34	4.30
14	4.00	4.09	4.12	4.00	3.99	3.84	3.95	3.93	3.62	3.80	3.93	3.98
15	3.94	3.83	3.66	3.39	3.30	3.48	3.43	3.29	3.24	3.63	3.91	3.96
16	3.96	3.83	3.51	3.16	2.95	2.86	2.96	3.03	3.18	3.69	4.09	4.08
17	4.09	4.02	3.63	3.20	2.93	2.80	2.86	2.97	3.25	3.82	4.16	4.15
18	4.01	4.05	3.70	3.31	2.99	2.76	2.85	3.00	3.27	3.74	4.05	4.07
19	3.95	3.93	3.61	3.24	3.01	2.82	2.81	2.97	3.23	3.62	3.88	3.96
20	3.81	3.78	3.46	3.18	2.92	2.69	2.78	2.89	3.14	3.44	3.70	3.83
21	3.73	3.67	3.39	3.13	2.91	2.74	2.71	2.85	3.08	3.36	3.57	3.71
22	3.64	3.54	3.33	3.14	2.98	2.79	2.80	2.86	3.08	3.27	3.45	3.62
23	3.60	3.48	3.33	3.29	3.18	3.10	3.04	2.98	3.17	3.26	3.41	3.56

677